

Article

Extreme Alteration of Chevkinite-(Ce) by Pb-CO₂-Rich Fluids: Evidence from the White Tundra Pegmatite, Keivy Massif, Kola Peninsula

Ray Macdonald ^{1,2}, Bogusław Bagiński ^{1,*}, Marcin Stachowicz ¹, Dmitry Zozulya ³, Jakub Kotowski ¹ and Petras Jokubauskas ¹

¹ Department of Geology, Mineralogy and Petrology, University of Warsaw, 02-089 Warsaw, Poland; raymacdonald186@gmail.com (R.M.); marcin.stachowicz@uw.edu.pl (M.S.); j.kotowski@uw.edu.pl (J.K.); p.jokubauskas@uw.edu.pl (P.J.)

² Environment Centre, University of Lancaster, Lancaster LA1 4YQ, UK

³ Geological Institute, Kola Science Centre, 14 Fersman Str., 184209 Apatity, Russia; dmitry.r.zozulya@gmail.com

* Correspondence: b.baginski1@uw.edu.pl; Tel.: +48-609-037-389

Abstract: An unusual hydrothermal alteration scheme was presented for chevkinite-(Ce) from the White Tundra pegmatite (2656 ± 5 Ma), Keivy massif, Kola Peninsula. Pb-CO₂-rich fluids initially removed REE and Y from the chevkinite-(Ce), with enrichment in Pb and U. PbO abundances reaching 17.35 wt%. Continued alteration resulted in the altered chevkinite-(Ce) being progressively transformed to a Pb-Ti-Fe-Si phase, which proved, upon EBSD analysis, to be almost totally amorphous. Pb enrichment was accompanied by a loss of LREE, especially La, relative to HREE, and the development of strong positive Ce anomalies. A notably U-rich aeschynite-(Y), with UO₂ values ≤ 7.67 wt%, crystallized along with the chevkinite-(Ce). Aeschynite-(Y) with a lower UO₂ value (3.91 wt%) and bastnäsite-(Ce) formed during alteration. The formation of bastnäsite-(Ce) rather than cerussite, which might have been expected in a high Pb-CO₂ environment, is ascribed to the fluids being acidic.

Keywords: White Tundra pegmatite; Pb-rich chevkinite-(Ce); CO₂-bearing hydrothermal fluids; amorphous Pb-Ti-Fe-Si phase



Citation: Macdonald, R.; Bagiński, B.; Stachowicz, M.; Zozulya, D.; Kotowski, J.; Jokubauskas, P. Extreme Alteration of Chevkinite-(Ce) by Pb-CO₂-Rich Fluids: Evidence from the White Tundra Pegmatite, Keivy Massif, Kola Peninsula. *Minerals* **2022**, *12*, 989. <https://doi.org/10.3390/min12080989>

Academic Editors: Harald G. Dill, Panagiotis Voudouris and Leonid Dubrovinsky

Received: 23 June 2022

Accepted: 27 July 2022

Published: 3 August 2022

Publisher's Note: MDPI stays neutral with regard to jurisdictional claims in published maps and institutional affiliations.



Copyright: © 2022 by the authors. Licensee MDPI, Basel, Switzerland. This article is an open access article distributed under the terms and conditions of the Creative Commons Attribution (CC BY) license (<https://creativecommons.org/licenses/by/4.0/>).

1. Introduction

The chevkinite-group minerals (CGM) are dominantly monoclinic REE-Ti-Fe sorosilicates $[(\text{REE},\text{Ca})_4\text{Fe}^{2+}(\text{Fe}^{2+},\text{Fe}^{3+},\text{Ti})_2\text{Ti}_2(\text{Si}_2\text{O}_7)_2\text{O}_8]$, but members with dominant Mg, Al, Mn, Cr, Sr, W, or Zr in one of the cation sites are also known. REE₂O₃ contents are up to ~50 wt% and, like other REE-bearing accessory minerals, the CGM are prone to alteration by hydrothermal fluids. Macdonald et al. [1] summarized some of the various alteration schemes and products of CGM alteration, showing that they are dependent on the compositions of the host rock and CGM, the composition and aggression of the fluids, in particular the activities of Ca, F, and CO₂, and to a lesser degree the temperature and pressure.

During our ongoing studies of mineralized occurrences in the Keivy alkaline province, we analyzed, in a pegmatite body, members of the chevkinite group. Textural and mineral chemical data from the body record the transition from pristine chevkinite-(Ce) to partly altered chevkinite-(Ce) containing unusually high contents of Pb (≤ 17.35 wt% PbO), and then to an enigmatic Pb-Ti-Fe-Si phase, which is accompanied by aeschynite-(Y), bastnäsite-(Ce), and quartz. The Pb-Ti-Fe-Si phase is thought to be a result of the almost complete alteration of chevkinite-(Ce) by Pb-rich, F-poor, carbonate-bearing fluids, a previously undescribed alteration scheme for the chevkinite group.

The specific aims of the study were to (i) document the progressive alteration of chevkinite-(Ce) to the Pb-Ti-Fe-Si phase; (ii) record the formation during the early stages of

alteration of an unusually Pb-rich chevkinite-(Ce); (iii) examine the nature of the Pb-Ti-Fe-Si phase by an electron back-scattered diffraction (EBSD) study; and (iv) comment on the nature of the hydrothermal fluids.

2. White Tundra Pegmatite

Dozens of pegmatite bodies in the Keivy province are confined to the inner and outer apical parts of alkali granite intrusions (Figure 1). Undoubtedly, these A-type granites are the source of the pegmatites. The body studied here, the White Tundra pegmatite (2656 ± 5 Ma; Lyalina et al. [2]), is elongated (2×5 m) and asymmetrical, with a quartz-rich core enveloped by a coarse-grained quartz-riebeckite/arfvedsonite (+/- feldspar) rock with abundant (locally up to 30–40 vol%) Zr-Y-REE-Nb-Th-Ti mineralization and finally rimmed by a pegmatitic lepidomelane-arfvedsonite granite. The pegmatite belongs to the earliest post-magmatic stage of the granite. It has been called Zirkonovoye for its high content of zircon, up to 30 vol%. Voloshin et al. [3] and Lyalina et al. [4] divided the body into five zones, reflecting its mineralogical diversity (Figure 1); however, the lack of continuous exposure makes the boundaries between the zones rather speculative. The sample studied here, 7-3-2, comes from the western part of the zone termed “pegmatite enriched in astrophyllite”.

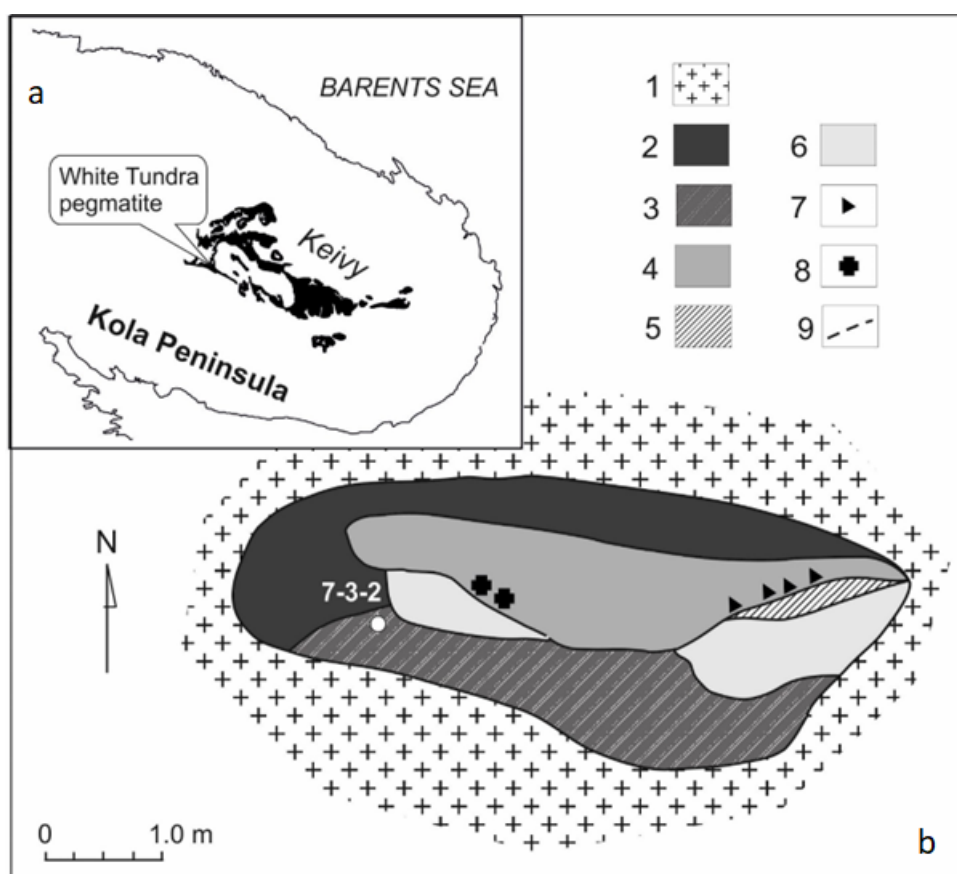


Figure 1. (a) Location of the White Tundra pegmatite in the Keivy alkaline province, Kola Peninsula. (b) Zones based on mineral assemblages in the pegmatite, 1—arfvedsonite-aegirine granite; 2—pegmatitic granite; 3—pegmatite, enriched in astrophyllite; 4—pegmatite, enriched in zircon, galena, and astrophyllite; 5—zone of secondary Y-REE mineralization; 6—quartz zone; 7—parts of maximum (up to 30 vol%) zircon content; 8—schlieren of galena; 9—zone boundaries. Modified after Lyalina et al. [4].

In addition to astrophyllite, titanite, chevkinite-(Ce), gadolinite-(Y), hingganite-(Y) and britholite-group minerals, the pegmatite is characterized by abundant galena and secondary

REE mineralization (tengerite-(Y), bastnäsite-(Y)) and rare-metal mineralization (zircon, fergusonite-(Y), thorite, monazite-(Ce), allanite-(Ce), and kainosite-(Y)). From a compilation of several earlier studies, Voloshin et al. [3], Lyalina et al. [2,4], and Zozulya et al. [5] suggested that the crystallization sequence of the main REE and HFSE minerals and titanisilicates in the pegmatite was: zircon–fergusonite–(Y)–monazite–(Ce)–astrophyllite–titaniate–allanite–(Ce)–britholite–(Y)–chevkinite–(Ce)–kainosite–(Y)–REE carbonates. Zone 3, which hosts our study specimen, is composed mainly of coarse-grained quartz (80–90 vol%) and amphibole (riebeckite) (10–15 vol%), with astrophyllite about 3–5 vol.%. Galena forms scarce rounded grains. A remarkable feature of the pegmatite is the occurrence of quartz–zircon aggregates forming spherules and rarely elongated linear intergrowths (Voloshin et al. [3]). The mineral paragenesis and distinctive shape of the aggregates point to a pseudomorphic nature. Voloshin et al. [3] proposed eudialyte/elpidite/gittinsite as the precursor minerals replaced by zircon and quartz. The rocks are highly fragmented, making a complete petrographic description rather difficult.

3. Analytical Methods

Carbon-coated grain mounts were first examined using high-contrast BSE imaging with an accelerating voltage of 20 kV and a focused electron beam. Detailed imaging at high magnifications and preliminary phase identification were performed using a ZEISS AURIGA 60 FE (field emission) scanning electron microscope equipped with two Bruker XFlash 6|30 energy-dispersive silicon drift detectors (SDD EDS). Additionally, element maps of the whole sample, as well as comprehensive maps of selected areas of interest, were made using a ZEISS SIGMA VP FE (variable pressure, field emission) SEM equipped with automated stage and two Bruker XFlash 6|10 EDS detectors with an accelerating voltage of 20 kV.

Selected crystals were analyzed with a Cameca SXFiveFE at the electron microprobe laboratory in the Faculty of Geology, University of Warsaw. Samples were cleaned and precisely re-carbon coated (~20 nm) prior to analysis with a carbon coater (Leica EM ACE200) in pulse mode using a single carbon thread. In this way, the composite carbon coating could withstand an intensive electron beam for an extended analytical time; internal laboratory experiments showed a repeatable withstandability of 200 nA/10 min. All measurements were conducted with an electron beam of 15 kV. The beam currents were chosen on a point-basis depending on the mineral type and size. The minimal current was 20 nA; such a beam was used for analyses of small grains. A 75 nA beam was used to analyze chevkinite–(Ce),

Fluorine was determined in the CGM at levels up to 0.21 wt%. Belkin et al. [6] argued that the F values determined by electron microprobe represent interference between the F-K α ($\lambda = 18.3199 \text{ \AA}$) and Ce-M ξ ($\lambda = 18.3499 \text{ \AA}$) peaks. We acknowledge the uncertainty as to whether or not the reported F values are an artefact.

Electron back-scattered diffraction (EBSD) is complementary to compositional analysis (EDS, WDS) in delivering structural information on crystals. Collected frames are fitted to patterns that are calculated from a database of crystal structures. The unique diffraction features allow differentiation of phases, including polymorphs. Here we used EBSD to identify the stages of breakdown of the chevkinite–(Ce), i.e., the loss of crystallinity and the nature of the product Pb-Ti-Fe-Si phase. The experiments were carried out at the Nanolab, Faculty of Geology, University of Warsaw.

Before EBSD examination, the sample was additionally polished (using a vibrating polisher) for 12 h in a diamond suspension with a grain diameter of 1/4 micron. The sample was covered with a 4.4 nm carbon layer for better surface discharge. EBSD patterns were collected with a Zeiss Auriga electron microscope equipped with a Bruker e[−] FlashHR+ detector with an integrated ARGUS imaging device. The sample was tilted to 70° using the dedicated stage (tilt about sample X-axis) for an optimal EBSD signal with the working distance set to 22.8 mm, while the detector tilt angle was 1.7° and the sample-to-detector distance was (a) 15.94; (b) 15.74; (c) 15.17 mm. The experiment was carried out using an elec-

tron beam with an energy of 15 keV. Image tilt correction was used with the Zeiss SmartSEM software and no image rotation was applied. Each EBSD pattern of 800×600 resolution was recorded from (a) $0.82 \times 0.82 \mu\text{m}$; (b) $0.54 \times 0.54 \mu\text{m}$; (c) $1.17 \times 1.17 \mu\text{m}$ pixel areas during 300 ms and averaged from 3 collected frames. The system was calibrated in Bruker ESPRIT 2.1. All the collected patterns were compared to theoretical, simulated Kikuchi lines generated by the Esprit 2.2 software. Representative electron backscatter patterns of chevkinite-(Ce) were collected for the areas shown in Figure 2A,B. They are presented together with indexed, simulated patterns in Supplementary Figure S1. The altered phase (Groups 3 and 4 in Figure 2A,B) did not show any diffraction signal.

Table 1. Representative compositions of chevkinite-(Ce) and partly altered chevkinite.

Table 1. Cont.

Anal. no.	Group 1				Group 2			
	14	17	18	20	15	16	21	26
Gd	0.05	0.06	0.06	0.07	0.04	0.05	0.05	0.03
Dy	0.00	0.01	0.01	0.01	0.01	0.00	0.01	0.02
Sum A	3.94	3.97	4.01	4.02	3.44	3.75	3.56	3.22
Fe ²⁺ (=B)	1.00	1.00	1.00	1.00	1.00	1.00	1.00	1.00
Mn	0.11	0.10	0.11	0.13	0.07	0.09	0.08	0.04
Nb	0.05	0.04	0.02	0.02	0.06	0.06	0.03	0.10
Al	0.00	0.01	0.01	0.01	0.02	0.01	0.02	
Ti	0.94	1.06	0.88	0.86	1.74	1.24	1.80	2.34
Fe ²⁺	0.95	1.01	1.10	1.06	0.96	0.91	1.08	1.21
Sum C	2.04	2.22	2.11	2.09	2.85	2.32	3.00	3.69
Ti (=D)	2.00	2.00	2.00	2.00	2.00	2.00	2.00	2.00
P	0.00	0.01	0.00	0.00	0.06	0.02	0.04	
Si	4.07	3.89	3.99	3.99	3.65	3.95	3.54	3.27
Sum T	4.07	3.90	3.99	3.99	3.71	3.97	3.58	3.27
F	0.04	0.08	0.05	0.05	0.07	0.04	0.08	0.06
Σ cations	13.05	13.09	13.11	13.10	13.00	13.04	13.14	13.19

FeO*: all Fe as Fe²⁺; b.d., below detection; n.a., not analyzed.**Table 2.** Compositions of Pb-Ti-Fe-Si phase.

Anal.no.	Group 3				Group 4			
	22	23	24	25	8	9	10	12
wt%								
Nb ₂ O ₅	1.98	2.13	3.19	2.96	2.14	2.17	1.66	2.13
Ta ₂ O ₅	0.08	0.13	0.17	0.17	0.15	0.19	0.14	0.18
SiO ₂	6.69	6.75	6.81	7.70	9.23	9.3	9.18	9.88
TiO ₂	30.37	31.36	29.52	31.11	34.48	33.35	31.81	35.17
HfO ₂	0.29	0.29	0.26	0.25	0.26	0.28	0.27	0.29
ThO ₂	0.67	0.46	0.49	0.31	0.49	0.68	0.43	0.75
UO ₂	0.85	0.81	1.10	1.19	1.36	1.32	0.94	1.52
Fe ₂ O ₃ *	10.60	10.58	5.43	6.14	7.39	6.91	13.94	5.54
Y ₂ O ₃	0.37	0.30	0.41	0.57	0.78	0.67	0.48	0.83
La ₂ O ₃	0.86	0.54	0.21	0.20	0.25	0.22	0.21	0.26
Ce ₂ O ₃	3.34	2.43	2.39	2.10	2.14	2.1	1.75	2.22
Pr ₂ O ₃	0.37	0.22	0.18	0.20	0.27	0.22	0.16	0.24
Nd ₂ O ₃	1.54	0.94	0.78	0.87	1.08	0.89	0.87	1.18
Sm ₂ O ₃	0.33	0.24	0.25	0.43	0.35	0.4	0.37	0.44
Eu ₂ O ₃	0.07	b.d.	b.d.	b.d.	b.d.	b.d.	b.d.	b.d.
Gd ₂ O ₃	0.20	0.22	0.16	0.21	0.34	0.26	0.21	0.37
Tb ₂ O ₃	b.d.	b.d.	b.d.	b.d.	b.d.	b.d.	b.d.	b.d.
Dy ₂ O ₃	b.d.	b.d.	0.17	0.28	0.31	0.29	0.24	0.33
Ho ₂ O ₃	b.d.	b.d.	b.d.	b.d.	b.d.	b.d.	b.d.	b.d.
Er ₂ O ₃	b.d.	b.d.	b.d.	0.16	0.27	0.2	b.d.	0.18
Tm ₂ O ₃	b.d.	b.d.	b.d.	b.d.	b.d.	b.d.	b.d.	b.d.
Yb ₂ O ₃	0.14	0.12	0.18	0.17	0.24	0.18	0.14	0.2
Lu ₂ O ₃	b.d.	b.d.	b.d.	b.d.	b.d.	b.d.	b.d.	b.d.
WO ₃	0.69	0.70	0.72	0.81	0.89	0.8	0.8	0.88
CaO	0.22	0.22	0.10	0.10	0.04	0.03	b.d.	0.03
MnO	b.d.	b.d.	b.d.	b.d.	b.d.	b.d.	b.d.	b.d.
PbO	23.58	24.24	25.90	26.14	28.07	27.42	24.77	29.11
Na ₂ O	b.d.	b.d.	b.d.	b.d.	0.05	0.08	0.1	b.d.
K ₂ O	b.d.	0.02	0.03	b.d.	0.05	0.04	0.04	0.03

Table 2. Cont.

Anal.no.	Group 3				Group 4			
	22	23	24	25	8	9	10	12
F	0.21	0.12	0.13	b.d.	0.11	0.11	b.d.	0.16
Cl	0.22	0.20	0.19	0.11	0.02	b.d.	b.d.	b.d.
Sum	83.67	83.02	78.77	82.18	90.76	88.11	88.51	91.92
O ≡ F,Cl	0.22	0.20	0.19	0.11	0.02	b.d.	b.d.	b.d.
	83.67	83.02	78.77	82.18	90.76	88.11	88.51	91.92
Formulae on the basis of 22 oxygens								
Nb	0.23	0.25	0.40	0.35	0.23	0.24	0.18	0.22
Ta	0.01	0.01	0.01	0.01	0.01	0.01	0.01	0.01
Si	1.72	1.73	1.89	2.02	2.16	2.24	2.14	2.30
Ti	5.87	6.03	6.17	6.14	6.08	6.04	5.58	6.15
Hf	0.02	0.02	0.02	0.02	0.02	0.02	0.02	0.02
Th	0.04	0.03	0.03	0.02	0.03	0.04	0.02	0.04
U	0.05	0.05	0.07	0.07	0.07	0.07	0.05	0.08
Fe ³⁺	2.05	2.04	1.14	1.21	1.30	1.25	2.45	0.97
Y	0.05	0.04	0.06	0.08	0.10	0.09	0.06	0.10
La	0.08	0.05	0.02	0.02	0.02	0.02	0.02	0.02
Ce	0.31	0.23	0.24	0.20	0.18	0.19	0.15	0.19
Pr	0.03	0.02	0.02	0.02	0.02	0.02	0.01	0.02
Nd	0.14	0.09	0.08	0.08	0.09	0.08	0.07	0.10
Sm	0.03	0.02	0.02	0.04	0.03	0.03	0.03	0.04
Eu	0.01							
Gd	0.02	0.02	0.01	0.02	0.03	0.02	0.02	0.03
Tb								
Dy			0.02	0.02	0.02	0.02	0.02	0.02
Ho								
Er				0.01	0.02	0.02		0.01
Tm								
Yb	0.01	0.01	0.02	0.01	0.02	0.01	0.01	0.01
Lu								
W	0.03	0.03	0.03	0.03	0.03	0.03	0.03	0.03
Ca	0.06	0.06	0.03	0.03	0.01	0.01		0.01
Mn								
Pb	1.63	1.67	1.94	1.85	1.77	1.78	1.56	1.82
Na					0.02	0.04	0.05	
K		0.01	0.01		0.01	0.01	0.01	0.01
F	0.17	0.10	0.11	0.00	0.08	0.08		0.12
Cl	0.10	0.09	0.09	0.05	0.01			
Σ cations	12.39	12.37	12.23	12.25	12.28	12.27	12.47	12.20
Sum A	2.47	2.37	2.64	2.55	2.54	2.51	2.14	2.60
	1.65	1.62	1.66	1.62	1.62	1.62	1.57	1.62
Fe ²⁺ (=B)	1.69	1.66	1.70	1.66	1.67	1.66	1.60	1.67
	1.74	1.70	1.75	1.71	1.71	1.70	1.64	1.71
Fe ³⁺	1.78	1.75	1.79	1.75	1.75	1.74	1.68	1.75
Mn	1.82	1.79	1.84	1.79	1.79	1.79	1.72	1.79
Nb	1.86	1.83	1.88	1.83	1.84	1.83	1.76	1.84
Ta	1.91	1.87	1.93	1.88	1.88	1.87	1.80	1.88
W	1.95	1.91	1.97	1.92	1.92	1.91	1.84	1.92
Hf	1.99	1.96	2.01	1.96	1.96	1.95	1.88	1.96
Ti	2.04	2.00	2.06	2.00	2.01	2.00	1.92	2.01
Sum C	2.08	2.04	2.10	2.04	2.05	2.04	1.96	2.05
	2.12	2.08	2.15	2.09	2.09	2.08	2.00	2.09
Ti (=D)	2.17	2.12	2.19	2.13	2.13	2.12	2.04	2.13
	2.21	2.17	2.23	2.17	2.17	2.16	2.08	2.17
Si	2.25	2.21	2.28	2.21	2.22	2.21	2.12	2.22
	2.30	2.25	2.32	2.26	2.26	2.25	2.16	2.26
Σ cations	2.34	2.29	2.37	2.30	2.30	2.29	2.20	2.30

FeO*: all Fe as Fe²⁺; b.d., below detection.

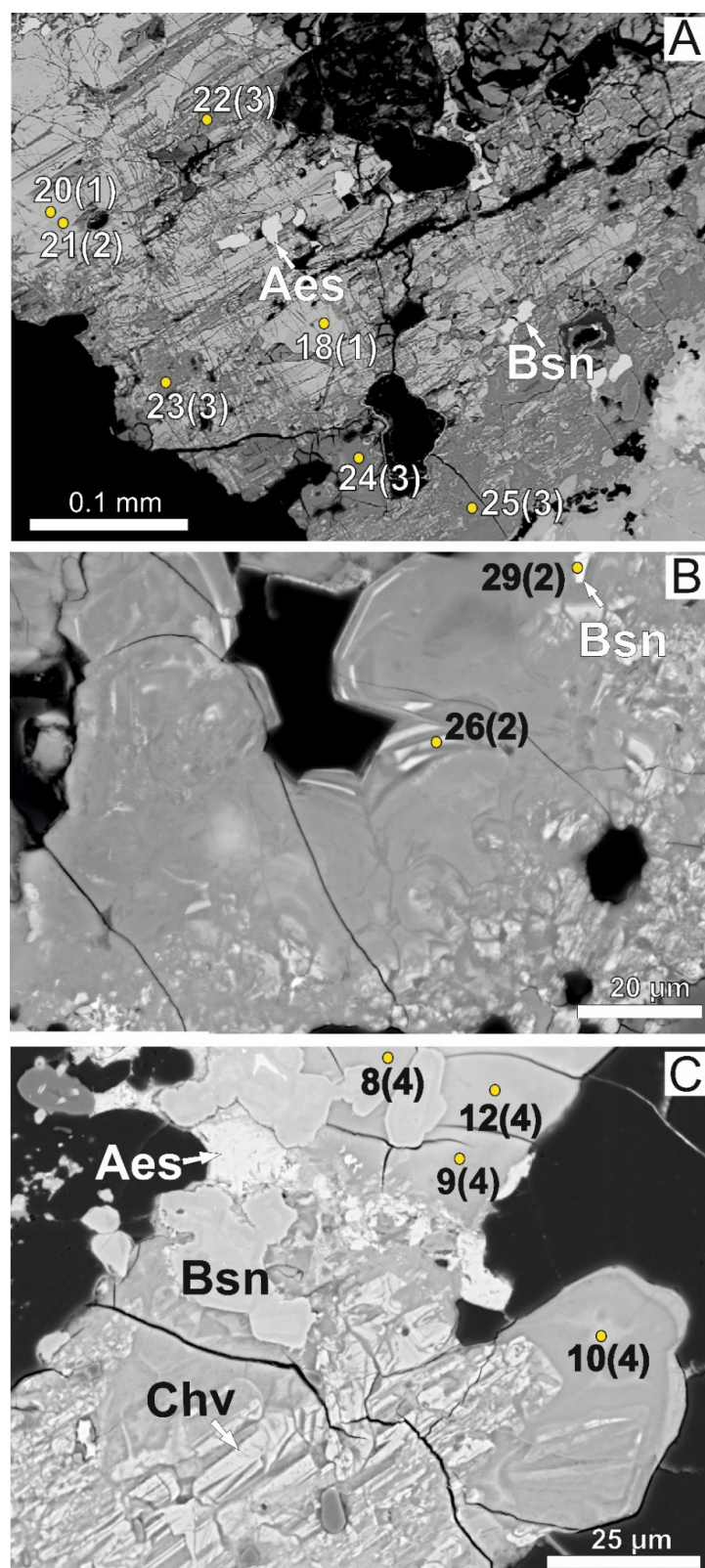


Figure 2. BSE images of textural relationships between Groups. (A) Striped zone consists of linear strips and small patches of Groups 1 and 2. Group 3 forms dark grey areas (e.g., bottom right), containing pale remnants of Groups 1 and 2. Spots show group and analysis number in Tables 1 and 2. (B) The main, pale grey area is Group 3, containing multiple remnants of Group 2. (C) Striped area (bottom left) breaks up to the right and eventually forms the pale “pseudo-homogeneous” grey areas (Group 4). Aes, aeschynite-(Y), Bsn, bastnäsite-(Ce).

4. Petrography

The CGM formed platy crystals showing variable degrees of alteration. In Figure 2A, the central striped zone on the left-hand side of the image consists of chevkinite-(Ce), forming pale patches and strips a few microns across (termed Group 1), which are intergrown with a slightly less bright phase which forms strips and larger, irregular patches (Group 2). Numbered spots show the group (in brackets) and the analysis number in Tables 1 and 2. The proportion of the grey phase to chevkinite-(Ce) locally increased until the chevkinite-(Ce) formed patches and elongated strips (some arcuate) immersed in a dark grey material, especially in the lower right part of the image (Group 3). The main, pale grey phase in Figure 2B is Group 3, in which there are multiple remnants of chevkinite. One arcuate strip (26) is from Group 2. The bottom left part of Figure 2C retains some features of the striped area in Figure 2A, with the stripes becoming increasingly broken up. Chevkinite inclusions became less common until, at the top and bottom right, the material formed pale grey areas which may, at a cursory glance, appear to be homogeneous (areas 9 and 12).

Bastnäsite-(Ce) is associated with the alteration of chevkinite-(Ce), ranging in form from to pale strips 20 μm long (Figure 2B) to irregular patches up to 10 μm across (Figure 2C). Aeschynite-(Y) occurs in two main forms: as anhedral grains up to 10 μm across intergrown with chevkinite-(Ce), and as a patchily zoned, anhedral plate 20 \times 15 μm in size (Figure 2C). The second form clearly formed during the later stages of alteration. Quartz is interstitial between chevkinite-(Ce) grains and is also present as isolated anhedral grains.

A remarkable feature of the pegmatite is the occurrence of quartz–zircon aggregates forming spherules and rarely elongated linear intergrowths (Voloshin et al. [3]). The mineral paragenesis and distinctive shape of the aggregates point to a pseudomorphic nature. Voloshin et al. [3] proposed eudialyte/elpidite/gittinsite as the precursor minerals replaced by zircon and quartz.

5. Mineral Compositions

5.1. Chevkinite-(Ce)

Representative analyses of chevkinite-(Ce) are given in Table 1; the full data set is in Supplementary Table S1. The analyses are all chevkinite-(Ce) in the classificatory scheme of Macdonald et al. [7]. Two broad groups can be recognized which relate directly to the petrographic distinctions made above. Group 1 had compositions close to pristine chevkinite-(Ce); analytical totals were ≥ 98 wt% and formulae were close to stoichiometric, the cation sums being 13.0 to 13.2, close to the theoretical 13. The formula for analysis 14, for example, can be written as $(\text{Ce}_{1.70}\text{La}_{0.85}\text{Nd}_{0.74}\text{Pr}_{0.21}\text{Ca}_{0.13}\text{Sm}_{0.11}\text{Gd}_{0.05}\text{Y}_{0.05})_{3.9}\text{Fe}^{2+}(\text{Fe}^{2+}_{0.95}\text{Ti}_{0.94}\text{Mn}_{0.12})_{2.0}\text{Ti}_{2.0}(\text{Si}_2\text{O}_7)_{2.0}\text{O}_8$. Calcium levels were low (≤ 0.58 wt% CaO), at the lower end of the range in chevkinite reported in the compilation of 239 CGM analyses by Macdonald et al. [1]. PbO levels were in the range below detection to 2.19 wt%, the higher levels being unusually high for the CGM. For example, in their compilation, Macdonald et al. [1] reported a PbO range of 0–1.0 wt % (average 0.13 wt%; 0–0.06 apfu Pb). Thorium levels were below detection, while U was just above the detection limit (≤ 0.11 wt% UO₂). Chondrite-normalized REE patterns were LREE-enriched, with a steep drop from Gd to Dy (Figure 3). There were modest negative Ce anomalies (Ce/Ce^* 0.65–0.74). Europium data were available for only one analysis, which showed a strong negative anomaly (Eu/Eu^* 0.08).

Group 2 had higher contents of Ti, Nb, Pb, Th, U, and lower Si, Fe, and REE, especially La. Analytical totals were between 95.38 and 99.18 wt% (average 97.4 wt%) and several analyses were clearly not stoichiometric, in that the A-site occupancy was <4 and the C-site occupancy >2. The Pb contents (4.03–17.35 wt% PbO; Pb ≤ 1.06 apfu) were unique in the CGM. These features are consistent with the phase being partially altered chevkinite-(Ce) with the removal of Si, REE, and Y and enrichment in Pb, U, Ti, and Nb, as recorded, with the exception of Pb and U, in several examples of CGM alteration by Bagiński et al. [9]. Iron contents were similar in both groups. Chondrite-normalized REE patterns (Figure 3b) were strongly LREE-enriched, with negative Ce anomalies (Ce/Ce^* 0.65–0.74) similar to the first group. Europium anomalies (Eu/Eu^*) were in the range 0.09–0.30.

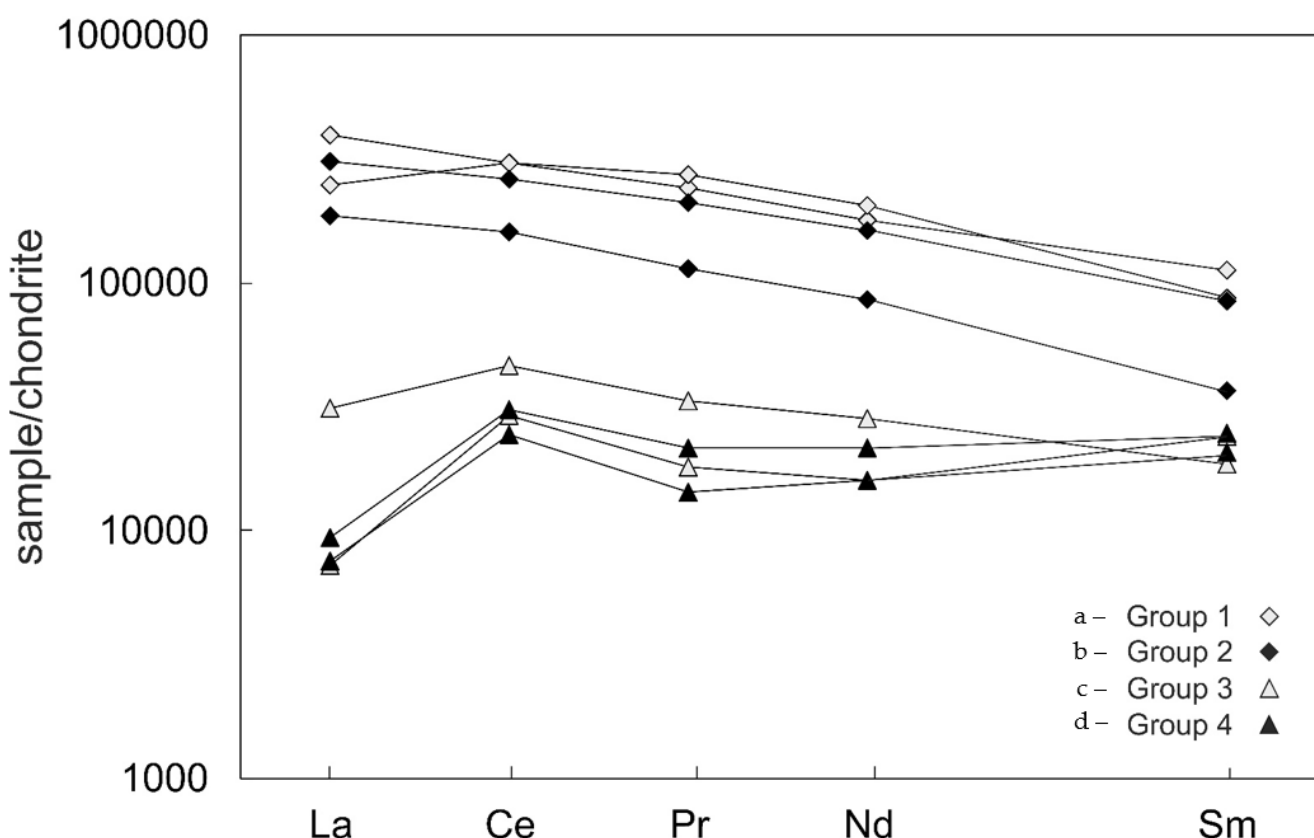


Figure 3. Chondrite-normalized REE patterns for (a) unaltered chevkinite-(Ce) (Group 1), (b) partially altered chevkinite-(Ce) (Group 2), (c) the Pb-Ti-Fe-Si phase (Group 3), and (d) the Pb-Ti-Fe-Si phase (Group 4). Normalization factors from Sun and McDonough [8].

5.2. Pb-Ti-Fe-Si Phase

Analyses of Groups 3 and 4 are given in Table 2. Analytical totals for both groups were low: Group 3, 78.8–83.7 wt% (average 81.9 wt%), Group 4, 88.1–91.9 (average 89.8 wt%). The dominant oxide was TiO_2 (29.5–35.2 wt %), followed by PbO (23.6–28.1 wt%), Fe_2O_3^* (5.4–10.6 wt%), SiO_2 (6.7–9.9 wt%), and Nb_2O_5 (1.7–3.2 wt%). Thorium levels were significant (up to 0.75 wt% ThO_2), and U levels were even higher (up to 1.52 wt% UO_2). Total $(\text{REE}+\text{Y})_2\text{O}_3$ contents were 4.4 to 7.2 wt%. La was removed more efficiently than Ce; La/Ce ratios were in the range 0.32–0.50 in Groups 1 and 2 chevkinite-(Ce) and 0.09–0.26 in the Pb-Ti-Fe-Si phase.

Chondrite-normalized REE patterns of Groups 3 and 4 (Figure 3a) showed, as a result of selective La removal, strong positive Ce anomalies ($\text{Ce}/\text{Ce}^* 1.45\text{--}3.02$). Patterns of the LREE heavier than Ce are variable, even within groups; $[\text{La}/\text{Nd}]_{\text{CN}}$ in Group 3 ranged from 0.45–1.13. This perhaps indicates that they were removed from the chevkinite-(Ce) in different proportions from different combinations of grains. $[\text{La}/\text{Nd}]_{\text{CN}}$ ratios in Groups 1 and 2 (1.2–2.2) were slightly higher than in Groups 3 and 4.

There were slight compositional differences between Groups 3 and 4. Group 3 had, on average, higher contents of Nb, La, Ce, Ca, and Cl and lower Si, Ti, Fe, Y, Sm-Er, Pb, and analytical totals. There were significant, if minor, amounts of W in both groups (0.69–0.81 and 0.80–0.89 wt% WO_3 , respectively). The only published determinations of W in chevkinite of which we are aware are those of Hussain et al. [10], who recorded W in the range 54.5–139 ppm in chevkinite-(Ce) in pegmatites of the Kohistan Batholith, Pakistan. Note, however, that the W end-member of the group, delhuyarite-(Ce), is known from the Nya Bastnäs deposit in Sweden (Holtstam et al. [11]). We are unaware of any mineral with the composition of the Pb-Ti-Fe-Si phase and suggest below that it formed by interaction of the chevkinite-(Ce) with a $\text{Pb}-\text{CO}_2$ -bearing fluid.

The relationship between the various textural forms of chevkinite and its alteration products can be seen on PbO plots (Figure 4). There was a strong positive correlation between PbO and TiO_2 (Fig. 4a), while that between PbO and $(\text{REE}+\text{Y})_2\text{O}_3$ was negative (Figure 4B). Silica values were rather constant until PbO is about 17 wt% and then dropped sharply to ~5 wt% SiO_2 (Figure 4D). FeO^* was constant through Groups 1 and 2 and then decreased. Groups 3 and 4 followed slightly different trends on the PbO- SiO_2 and PbO- FeO^* plots, which we ascribed above to variability in the proportion of Groups 1 and 2 in the alteration mix.

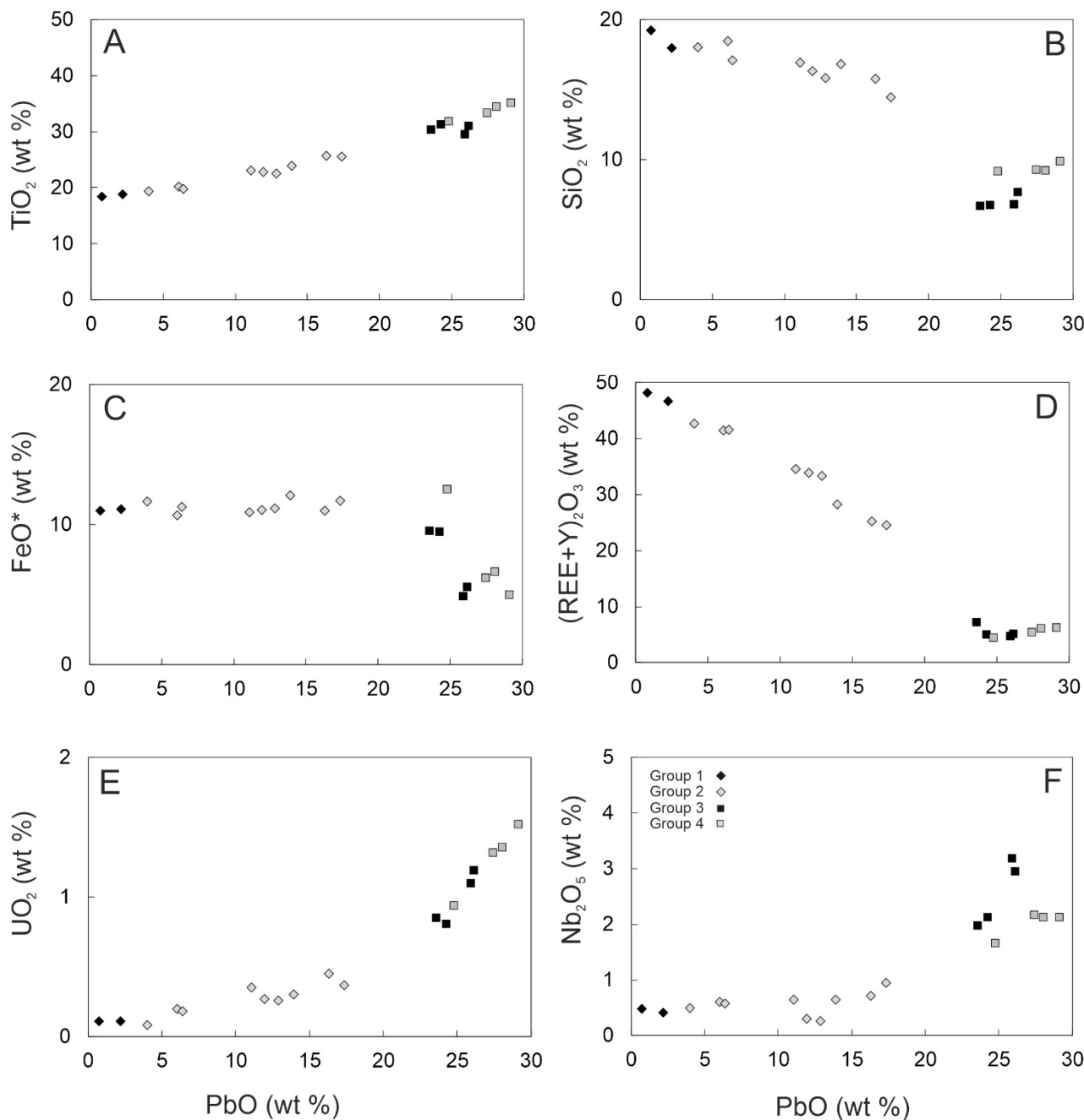


Figure 4. Compositional relationships between the groups shown on PbO v. (A) TiO_2 , (B) SiO_2 , (C) FeO^* , (D) $(\text{REE}+\text{Y})_2\text{O}_3$, (E) UO_2 , (F) Nb_2O_5 , (plots).

The distributions of Ce and Pb in the various textural zones are shown as Ce and Pb chemical maps in Figure 5, which covers the same area as in Figure 2A. The higher Ce contents (Figure 5A), shown in yellow and pink, represent Groups 1 and 2; Group 3 areas

are dark. The reverse distribution is shown by Pb (Figure 5B). Overall, the relationships showed that there was a fairly continuous transition between the unaltered chevkinite-(Ce) (Group 1) and the Pb-Ti-Fe-Si phase (Group 4), suggesting that they are all related to the same process.

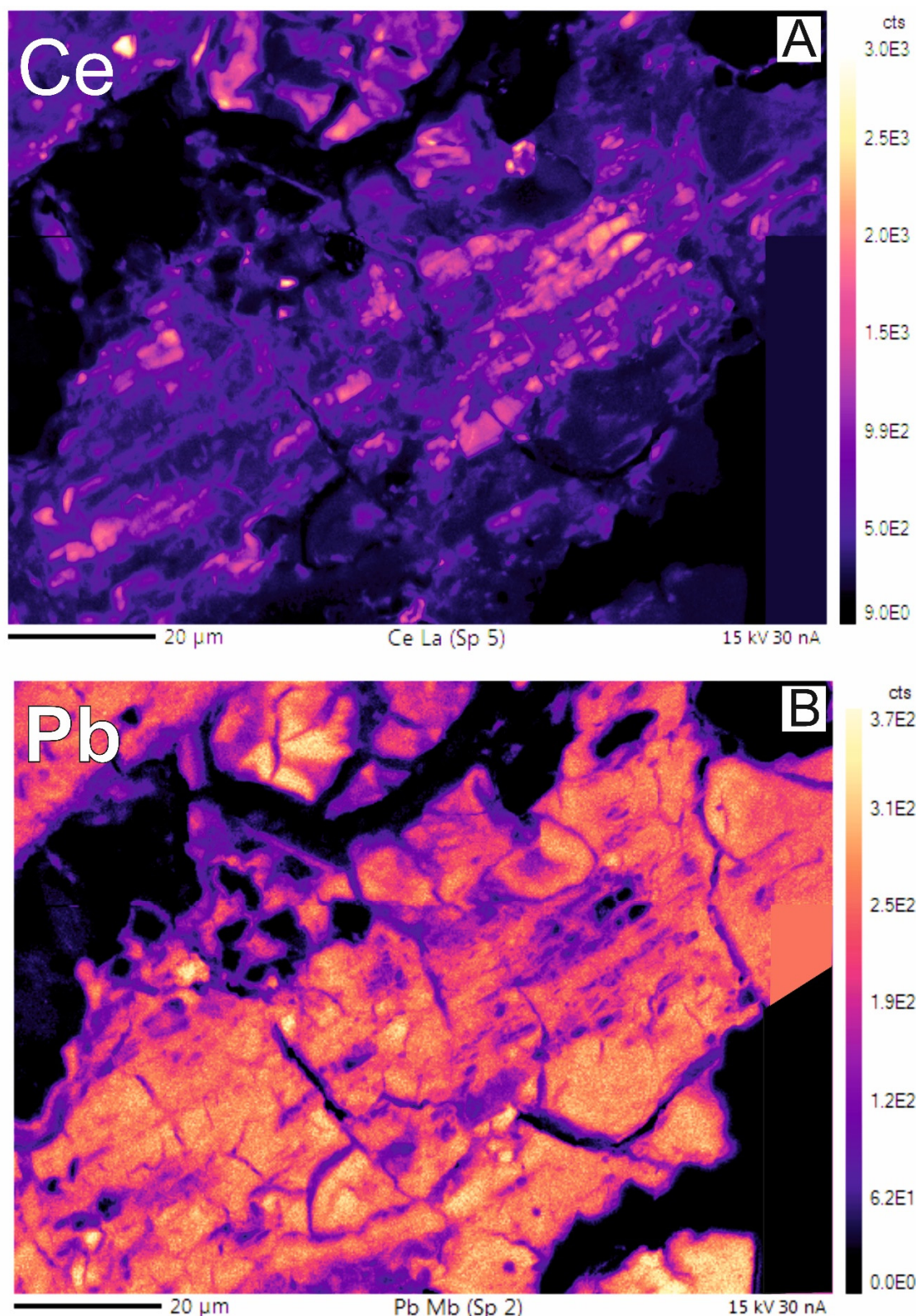


Figure 5. Chemical maps to show the antipathetic distribution of (A) Ce and (B) Pb.

5.3. Aeschynite-(Y)

The (REE,U,Th)-(Ti,Nb,Ta) oxide phase was classified as aeschynite-(Y) on the basis of the three-group canonical discriminant of Ercit [12] (Figure 6). Formulae were calculated on the basis of 3 cations, with all Fe as Fe^{3+} . Compositions and cation site allocations are given in Table 3, where some low analytical totals possibly indicate the presence of water. Aurisicchio et al. [13], for example, found both hydroxyl and molecular water, using infrared spectra, in aeschynite-(Y) from pegmatites from the Baveno pink granite, Italy. In Figure 6, analysis 11 can be seen to be rather different from analyses 1–5. In the latter, the A-site contains significant concentrations of HREE, Th, U, Pb, and Fe, with lesser abundances of Ca and Mn. Representative chondrite-normalized REE patterns (Figure 7) showed sharp increases from La to Gd, with negative Eu anomalies ($\text{Eu}/\text{Eu}^* = 0.19, 0.17$) and rather flat HREE. Uranium levels exceeded those of Th ($\text{Th}/\text{U} = 0.11\text{--}0.16$). The dominant cation in the B-site was Ti, with lesser amounts of Nb and Ta. A simplified average formula is: $[(\text{Y}_{0.45}\text{HREE}_{0.16}\text{Ca}_{0.14}\text{LREE}_{0.09}\text{U}_{0.08})_{0.92}(\text{Ti}_{1.28}\text{Nb}_{0.33}\text{Fe}^{3+}_{0.22}\text{Si}_{0.13}\text{Ta}_{0.06})_{2.02}(\text{O},\text{OH})_6]$. Analysis 11 contains higher Y and Ti and lower Nb and Ta than analyses 1–5; its formula can be written as $[(\text{Y}_{0.50}\text{HREE}_{0.19}\text{Ca}_{0.13}\text{LREE}_{0.07}\text{U}_{0.05})_{0.94}(\text{Ti}_{1.47}\text{Fe}^{3+}_{0.24}\text{Nb}_{0.23}\text{Ta}_{0.02})_{1.96}(\text{O},\text{OH})_6]$. The differences reflect the different textural positions: analyses 1–5 are from anhedral grains enclosed in chevkinite-(Ce); analysis 11 from the anhedral grain associated with Group 4 and presumably formed later.

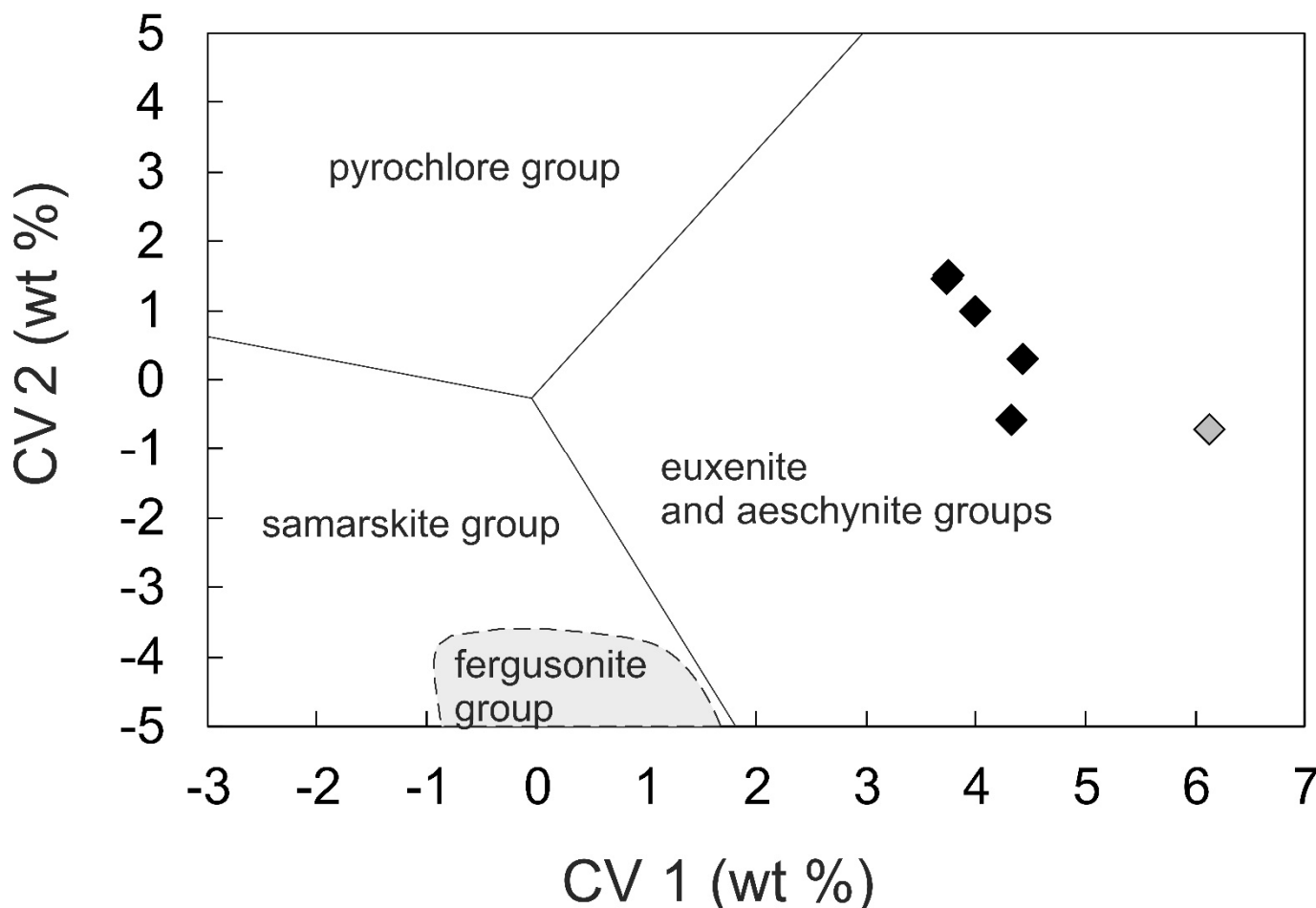


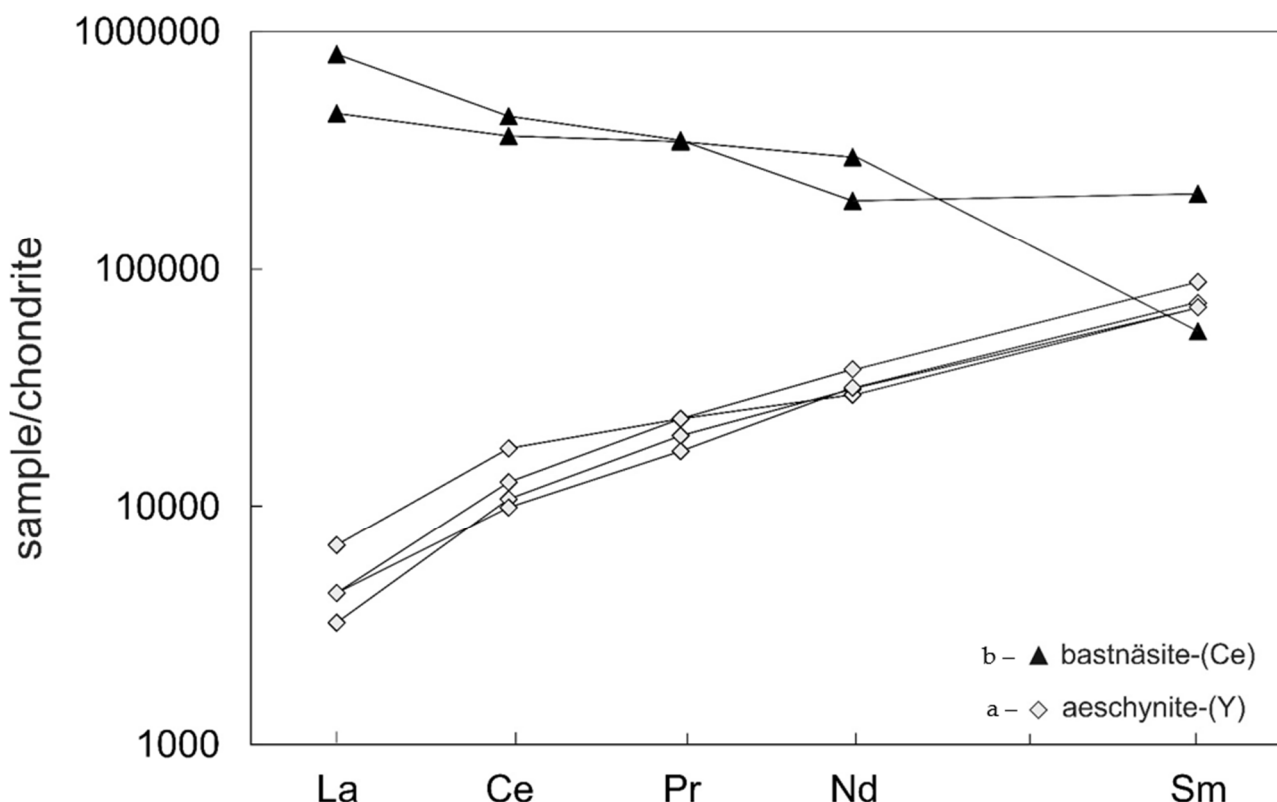
Figure 6. Aeschynite-(Y) plotted as canonical variables CV1 and CV2 of the three-group model of Ercit (2005). Data are from Table 3. $\text{CV1} = 0.245 \text{ Na} + 0.106 \text{ Na} + 0.106 \text{ Ca} - 0.077 \text{ Fe}^* + 0.425 \text{ Pb} + 0.220 \text{ Y} + 0.280 \text{ LREE} + 0.137 \text{ HREE} + 0.100 \text{ U}^* + 0.304 \text{ Ti} + 0.097 \text{ Nb} + 0.109 \text{ Ta}^* - 12.81$ (oxide wt%). $\text{CV2} = 0.102 \text{ Na} - 0.113 \text{ Ca} - 0.371 \text{ Fe}^* - 0.167 \text{ Pb} - 0.395 \text{ Y} - 0.280 \text{ LREE} - 0.265 \text{ HREE} - 0.182 \text{ U}^* - 0.085 \text{ Ti} - 0.166 \text{ Nb} - 0.146 \text{ Ta}^* + 17.29$ (wt%). $\text{Fe}^* = \text{Fe} + \text{Mn}$; $\text{U}^* = \text{U} + \text{Th}$; $\text{Ta}^* = \text{Ta} + \text{W}$.

Table 3. Compositions of aeschynite-(Y) and bastnäsite-(Ce).

Anal. no.	aeschynite-(Y)					bastnäsite-(Ce)		
	1	2	3	4	5	11	28	6
wt%								
Nb ₂ O ₅	13.81	13.92	12.03	12.79	13.99	9.14	0.15	b.d.
Ta ₂ O ₅	3.74	3.56	4.44	4.68	3.72	1.21	b.d.	b.d.
SiO ₂	2.65	1.94	3.52	3.97	0.21	0.69	2.15	1.32
TiO ₂	28.89	29.36	25.94	26.64	29.45	35.30	5.14	0.79
HfO ₂	0.18	0.23	0.23	0.21	0.22	0.31	b.d.	b.d.
ThO ₂	0.76	0.82	1.12	1.15	0.73	0.44	b.d.	b.d.
UO ₂	6.76	6.60	7.21	7.67	6.42	3.91	0.15	b.d.
Fe ₂ O ₃	4.71	5.05	4.56	3.54	7.28	5.65	2.92	1.69
Y ₂ O ₃	14.42	14.60	12.88	13.43	14.57	17.02	1.30	7.84
La ₂ O ₃	n.a.	0.09	0.19	0.16	0.12	0.12	22.38	12.61
Ce ₂ O ₃	0.80	0.77	1.26	1.03	0.71	0.91	31.82	25.96
Pr ₂ O ₃	n.a.	0.22	0.26	0.24	0.19	0.26	3.88	3.85
Nd ₂ O ₃	1.67	1.71	1.61	1.59	1.73	2.07	10.65	16.27
Sm ₂ O ₃	1.24	1.28	1.23	1.26	1.22	1.56	0.97	3.67
Eu ₂ O ₃	n.a.	b.d.	0.09	b.d.	b.d.	0.13	b.d.	0.53
Gd ₂ O ₃	2.24	2.25	2.09	2.21	2.13	2.68	0.57	3.39
Tb ₂ O ₃	n.a.	0.40	0.38	0.41	0.36	0.49	b.d.	0.25
Dy ₂ O ₃	2.72	2.69	2.59	2.73	2.93	2.95	b.d.	1.26
Ho ₂ O ₃	n.a.	0.36	0.39	0.51	0.38	0.32	b.d.	b.d.
Er ₂ O ₃	2.02	2.06	1.81	1.90	1.95	2.04	b.d.	0.43
Tm ₂ O ₃	n.a.	0.36	0.39	0.51	0.38	0.32	b.d.	b.d.
Yb ₂ O ₃	1.77	1.74	1.51	1.56	1.76	1.85	b.d.	0.22
Lu ₂ O ₃	n.a.	0.15	0.16	0.16	0.16	0.14	b.d.	b.d.
WO ₃	n.a.	0.17	0.22	0.12	0.18	0.19	0.19	0.08
CaO	2.16	2.32	2.16	1.71	2.90	2.22	0.82	1.13
MnO	0.17	0.18	0.12	0.13	0.36	0.19	b.d.	b.d.
PbO	0.48	0.46	1.93	0.79	0.52	0.62	2.86	1.14
Na ₂ O	0.09	0.05	0.09	0.13	b.d.	b.d.	b.d.	0.08
K ₂ O	b.d.	b.d.	b.d.	0.03	b.d.	b.d.	b.d.	b.d.
F	b.d.	b.d.	0.15	0.16	0.12	0.15	5.13	4.26
Cl	b.d.	b.d.	b.d.	b.d.	0.07	b.d.	0.04	0.09
Sum	91.28	93.34	90.56	91.42	94.76	92.88	91.12	86.86
O ≡ F, Cl	0.00	0.00	0.06	0.07	0.07	0.06	2.17	1.82
Total	91.28	93.34	90.50	91.35	94.69	92.82	88.95	85.04
Formulae on the basis of 3 cations								
1 cation basis								
Th	0.01	0.01	0.02	0.02	0.01	0.01		
U	0.09	0.08	0.10	0.10	0.08	0.05	0.00	
Ca	0.13	0.14	0.14	0.11	0.18	0.13	0.02	0.04
Y	0.45	0.45	0.41	0.43	0.44	0.50	0.02	0.12
La		0.00	0.00	0.00	0.00	0.00	0.23	0.14
Ce	0.02	0.02	0.03	0.02	0.01	0.02	0.32	0.28
Pr		0.00	0.01	0.01	0.00	0.01	0.04	0.04
Nd	0.03	0.04	0.03	0.03	0.04	0.04	0.10	0.17
Sm	0.02	0.03	0.03	0.03	0.02	0.03	0.01	0.04
Eu		0.00			0.00		0.01	
Gd	0.04	0.04	0.04	0.04	0.04	0.05	0.01	0.03
Tb	0.01	0.01	0.01	0.01	0.01	0.01		0.00
Dy	0.05	0.05	0.05	0.05	0.05	0.05		0.01
Ho	0.01	0.01	0.01	0.01	0.01	0.01		
Er	0.04	0.04	0.03	0.04	0.03	0.04		0.00
Tm	0.01	0.01	0.01	0.01	0.01	0.01		
Yb	0.03	0.03	0.03	0.03	0.03	0.03		0.00
Lu		0.00	0.00	0.00	0.00	0.00		
Mn	0.01	0.01	0.01	0.01	0.02	0.01		
Pb	0.01	0.01	0.03	0.01	0.01	0.01	0.02	0.01

Table 3. Cont.

Anal. no.	1	2	aeschynite-(Y)			bastnäsite-(Ce)		
			3	4	5	11	28	6
Na	0.01	0.01	0.01	0.02				0.00
K				0.00				
Sum A	0.95	0.97	0.99	0.98	1.00	1.00		
Nb	0.36	0.36	0.33	0.35	0.36	0.23	0.00	
Ta	0.06	0.06	0.07	0.08	0.06	0.02		
Si	0.15	0.11	0.21	0.24	0.01	0.04	0.06	0.04
Ti	1.27	1.27	1.18	1.20	1.26	1.47	0.11	0.02
Hf	0.00	0.00	0.00	0.00	0.00	0.00		
Fe ³⁺	0.21	0.22	0.21	0.16	0.31	0.24	0.06	0.04
W		0.00	0.00	0.00	0.00	0.00	0.00	0.00
Sum B	2.05	2.03	2.01	2.02	2.00	2.00	0.23	0.09
F	0.00	0.00	0.03	0.03	0.02	0.03	0.45	0.40
Cl					0.01		0.00	0.00

FeO*: all Fe as Fe²⁺; b.d., below detection; n.a., not analyzed.**Figure 7.** Chondrite-normalized REE plots for (a) aeschynite-(Y) and (b) bastnäsite-(Ce). Normalization factors from Sun and McDonough [8].

5.4. Bastnäsite-(Ce)

Two analyses of bastnäsite-(Ce) were conducted (Table 3). The high values of Ti, Nb \pm Fe in analysis 28 are almost certainly a result of beam contamination from the surrounding Pb-Ti-Fe-Si phase. The main differences between the two analyses are shown on a chondrite-normalized plot (Figure 7b). Analysis 28 was strongly LREE-enriched; Gd was the only HREE above detection limit. La did not show the same relative depletion as in the Pb-Ti-Fe-Si phase and aeschynite-(Y): $[La/Ce]_{cn} = 1.25, 1.81$. Analysis 6 was less strongly LREE-enriched, with a flatter pattern than Sm. There was a significant Eu anomaly ($Eu/Eu^* = 0.46$) and then further HREE depletion. Simplified compositions are arcuate strip

(analysis 28) $[(Ce_{0.42}La_{0.30}Nd_{0.14}Fe^{3+}_{0.08}Pr_{0.05})_1(OH_{0.55}F_{0.45})]$ and anhedral patch (analysis 6) $[(Ce_{0.31}Nd_{0.19}La_{0.16}Y_{0.13}Ca_{0.04}Pr_{0.04}Sm_{0.04}Fe^{3+}_{0.04}Gd_{0.03})_1(OH_{0.60}F_{0.40})]$.

6. Nature of the Pb-Ti-Fe-Si Phase

The decaying quality of collected EBSD patterns in Groups 1 to 4 reflects the progressive structural breakdown of the chevkinite-(Ce). All areas numbered in Figure 2 were tested. Groups 1 and 2 are crystalline chevkinites-(Ce) (Supplementary Figure S1a,b). Groups 3 and 4 did not give an electron diffraction signal. The breakdown destroyed the periodic arrangement of atoms in the crystal lattices (Supplementary Figure S1c,d). In Group 3, we observed crystalline fragments surrounding areas 22(3) 23(3), whereas in the more homogenous 24(3), we observed only one pixel spot of $1\ \mu m^2$ with weak diffraction lines (Supplementary Figure S1e), representing remnants of crystalline chevkinite-(Ce). In one area of Group 4 (9(4)), one pixel showed even weaker diffraction (Supplementary Figure S1f). The bastnäsite and aeschynite phases in Figure 2C are amorphous, and the chevkinite-(Ce) area is crystalline.

7. Discussion

7.1. Pb in the Structure of Group 2 Chevkinite-(Ce)

Pb values in Group 2 analyses were up to 1.1 apfu, i.e., about one-quarter of the A-site. The Pb was strongly negatively correlated with REE+Y (Figure 5B), raising the question as to whether it is replacing them in the structure and, if so, what was the charge-balancing replacement? By calculating Fe^{3+} and Fe^{2+} from stoichiometry (Supplementary Table S1), a possible reaction is as follows (Figure 8):

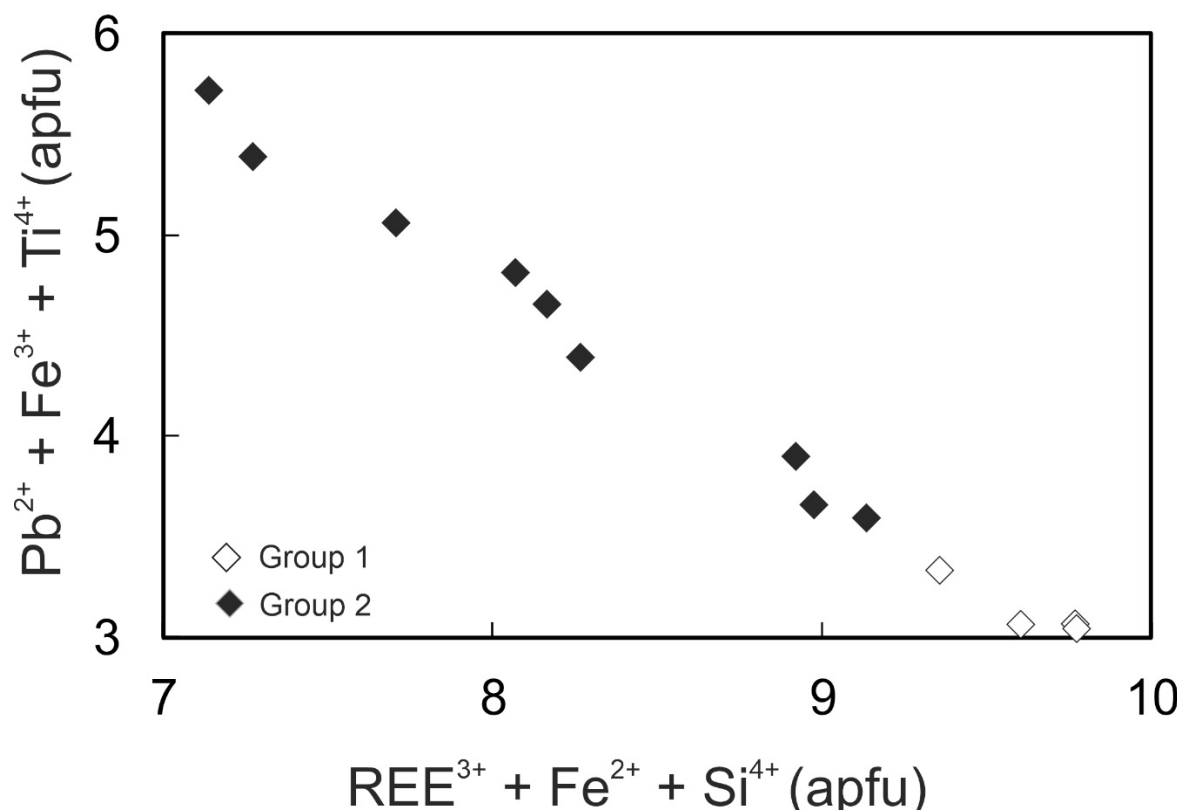
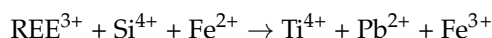
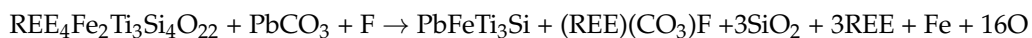


Figure 8. Possible substitution scheme for Pb-rich, partly altered, Group 2 chevkinite-(Ce).

This relationship between the major cations might suggest that any water incorporated into the Group 2 crystals is entirely interstitial and did not have an important structural role. Alternatively, the low analytical totals may be a result of vacancies in the structure.

7.2. The Alteration Mechanism

Given the composition of the Pb-Ti-Fe-Si phase and the fact that it is associated with aeschynite-(Y), bastnäsite-(Ce) and quartz, it is possible to suggest a relationship for its formation:



The HREE (+Y) and Fe released entered aeschynite-(Y). The LREE entered bastnäsite-(Ce) and the SiO₂ formed quartz. The reaction appears to have been strongly oxidizing. We note that Lyalina et al. [2] proposed oxidizing conditions during zircon crystallization in the pegmatite based on the presence of positive Ce anomalies in the zircon.

The compositional variations shown in Figure 4 can be used to speculate on the breakdown sequence. Between Groups 1 and 2, cation exchanges and losses involved mainly A-site cations (REE, U, Pb): Fe and Si contents were about constant. The loss of REE from the interlayer site in Kola Peninsula titanosilicates was referred to as “decationization of the interlayer population” by Ferraris [14], where ions with greater radii tend to leave the chevkinite structure first. By Group 3, all the cations were involved in the alteration, perhaps representing a major structural breakdown of the chevkinite-(Ce) to the amorphous material.

7.3. Hydrothermal Fluids

It is proposed here that the incorporation of Pb into the chevkinite-(Ce) and the formation of the Pb-Ti-Fe-Si phase were the result of interaction with a hydrous fluid phase containing CO₂ and F, the most direct empirical evidence being the formation of bastnäsite-(Ce). The loss of LREE relative to HREE in the chevkinite-(Ce) and aeschynite-(Y) as alteration proceeded is consistent with their greater solubility in CO₂-rich fluids (Smith et al. [15]). Earlier, Zozulya et al. [16] suggested, from their study of the britholite-group minerals, that they had crystallized at relatively high F activity and low CO₂/H₂O ratios. Zozulya et al. [5] found that fergusonite in the pegmatite has [La/Nd]_{cn} = 0.03–1.2, indicating relatively high H₂O/CO₂ in fluids. Such a fluid is consistent with theoretical studies that the REE form the most stable complexes with F and moderately strong complexes with CO₂ (Haas et al. [17]; Samson and Wood [18]). In comparison, Macdonald et al. [19] described, in a syenitic pegmatite from the Vishnevye Mountains, Russia, chevkinite-(Ce) being altered, via a series of texturally complex intermediate steps, to a bastnäsite-(Ce)-ilmenite-columbite-(Fe) assemblage. The hydrothermal fluids were inferred to have been F- and CO₂-rich, with variable levels of Ca activity. Li and Zhou [20] reported replacement of chevkinite-(Ce) by allanite-(Ce) + aeschynite-(Ce) ± bastnäsite-(Ce) ± columbite-(Fe) ± ilmenite at the Sin Quyen Fe-Cu-LREE-Au deposit, Vietnam. The White Tundra case differs from those cases in that, apart from minor aeschynite-(Y) and bastnäsite-(Ce), no major new mineral phase was formed; the breakdown of chevkinite-(Ce) resulted in an amorphous material.

The fluid carried significant amounts of W, which was incorporated into the Group 3 and 4 phases. As noted earlier, Groups 3 and 4 were enriched in Th and, particularly, U. The U showed an excellent positive correlation with Pb (Figure 5B), which had two segments. In the Group 2 analyses, they both increased with a constant Pb/U ratio; in Groups 3 and 4, U increased more rapidly than Pb, suggesting that it was more soluble in the fluid.

7.4. Significance for the White Tundra Pegmatite

We noted earlier that the White Tundra pegmatite is characterized by abundant galena and secondary REE mineralization (tengerite-(Y), bastnäsite-(Y)). The association in our sample of Pb with carbonate points to a local variant of the alteration mechanism, perhaps related to a separate influx of hydrothermal fluid(s).

The agpaitic to non-agpaitic transition during evolution of the pegmatite, e.g., zirconosilicates → zircon, astrophyllite → titanite assemblages, galena and molydenite mineralization, high contents of Sn and W in the minerals, suggests that the parental magma was contaminated by highly evolved Pb-Sn-W-Mo-enriched crustal lithologies. Contamination by host rocks has been established for Pb-rich amazonite pegmatites elsewhere, e.g., the Ploskaya Mountain, Kola Peninsula (Voloshin and Pakhomovskii [21], Broken Hill, Australia (Stevenson and Martin [22], and Madagascar (Martin et al. [23]). The unique Ploskaya Mt amazonite pegmatite intrudes the Keivy metavolcanic complex. It is several hundred meters long and several tens of meters wide. In addition to the distinct and significant Y, Nb, F mineralization, the presence of Li, Ta, Pb, Sn, and Mn minerals (anglesite, cassiterite, cerussite, galena, kasolite, kenoplumbomericrolite, molydenite, plumbopyrochlore, polylithionite, pyromorphite, and wulfenite) indicates a mixed NYF (Nb-Y-F)-LCT (Li-Cs-Ta) family. The geological setting and main geochemical features of the pegmatite point to its relationship to the Keivy alkaline granite. Formation of the pegmatite by remobilization of rare metals from an alkali granite and the host gneisses have been suggested by Zozulya et al. [24].

The high activities of Pb and CO₂ point to the formation of cerussite in this environment as a possible low-temperature product. The formation of cerussite is controlled mainly by the pH in alkaline conditions (Bao et al. [25]; El Alaoui and Dekayir [26]). Its absence from the White Tundra pegmatite points to an acidic environment, allowing the Pb to be transported in the fluids as ions and/or hydroxides. Alteration of the chevkinite-(Ce) resulted in the release of REE into the hydrothermal fluids and their replacement by Pb (Stage 2), with the subsequent crystallization of bastnäsite (Stages 3 and 4).

Supplementary Materials: The following supporting information can be downloaded at: <https://www.mdpi.com/article/10.3390/min12080989/s1>, Table S1: Compositions of chevkinite-(Ce) and altered chevkinite-(Ce) [27]. Figure S1 Representative EBSD patterns, together with simulated chevkinite-(Ce) indexed patterns for areas (a) 18(1) and (b) 26(2). Representative experimental images of areas (c) 25(3) and (d) 9(4), where no signal was detected. Exceptional EBSD patterns recorded were recorded in only one pixel of 1 μm² for area (e) 24 (3) and (f) 9 (4).

Author Contributions: Conceptualization, R.M. and B.B.; investigation, R.M., M.S. and D.Z.; resources, D.Z.; writing—original draft, R.M.; data curation, D.Z., J.K. and P.J.; writing—review and editing, M.S.; project administration, B.B.; formal analysis, P.J. All authors have read and agreed to the published version of the manuscript.

Funding: R.M.: B.B., M.S and P.J. gratefully acknowledge funding by NCN Harmonia grant no. 2017/26/M/ST10/00407. DZ acknowledges RSCF grant 22-17-20002 (<https://rscf.ru/project/22-17-20002>).

Data Availability Statement: Not applicable.

Acknowledgments: We thank the anonymous reviewers and the Academic Editor for very helpful comments on the manuscript.

Conflicts of Interest: The authors declare no conflict of interest.

References

- Macdonald, R.; Bagiński, B.; Belkin, H.E.; Stachowicz, M. Composition, paragenesis, and alteration of the chevkinite group of minerals. *Am. Mineral.* **2019**, *104*, 349–367. [[CrossRef](#)]
- Lyalina, L.M.; Zozulya, D.R.; Bayanova, T.B.; Selivanova, E.A.; Savchenko, Y.E.E. Genetic features of zircon from pegmatites of Neoarchean alkali granites in the Kola Region. *Zap. RMO* **2012**, *141*, 35–51. (In Russian)
- Voloshin, A.V.; Lyalina, L.M.; Savchenko, E.E.; Selivanova, E.A. Intragranite rare metal pegmatites in alkaline-granite formation of Kola Peninsula, quartz-zircon pseudomorphs. *Zap. RMO* **2005**, *4*, 98–108. (In Russian)
- Lyalina, L.M.; Selivanova, E.A.; Savchenko, Y.E.E.; Zozulya, D.R.; Kadyrova, G.I. Minerals of the gadolinite-(Y)—Hingganite-(Y) series in the alkali granite pegmatites of the Kola Peninsula. *Geol. Ore Depos.* **2014**, *56*, 675–684. [[CrossRef](#)]
- Zozulya, D.R.; Macdonald, R.; Bagiński, B. REE fractionation during crystallization and alteration of fergusonite-(Y) from Zr-REE-Nb-rich late- to post-magmatic products of the Keivy alkali granite complex, NW Russia. *Ore Geol. Rev.* **2020**, *125*, 103693. [[CrossRef](#)]

6. Belkin, H.E.; Macdonald, R.; Grew, E.S. Chevkinite-group minerals from granulite-facies metamorphic rocks and associated pegmatites of East Antarctica and South India. *Miner. Mag.* **2009**, *73*, 149–164. [[CrossRef](#)]
7. Macdonald, R.; Belkin, H.E.; Wall, F.; Bagiński, B. Compositional variation in the chevkinite group: New data from igneous and metamorphic rocks. *Miner. Mag.* **2009**, *73*, 777–796. [[CrossRef](#)]
8. Sun, S.S.; McDonough, W.F. Chemical and isotopic systematics of oceanic basalts: Implications for mantle composition and processes. *Geol. Soc. Lond. Spec. Publ.* **1989**, *42*, 13–345. [[CrossRef](#)]
9. Bagiński, B.; Macdonald, R.; Dzierżanowski, P.; Zozulya, D.; Kartashov, P.M. Hydrothermal alteration of chevkinite-group minerals. Part 1. Hydration of chevkinite-(Ce). *Miner. Mag.* **2015**, *79*, 1019–1037. [[CrossRef](#)]
10. Hussain, A.; Zhao, K.-D.; Arit, M.; Palmer, M.R.; Chen, W.; Zhang, Q.; Li, Q.; Jiang, S.-Y.; Girei, M.B. Geochronology, mineral chemistry and genesis of REE mineralization in alkaline rocks from the Kohistan Island Arc, Pakistan. *Ore Geol. Rev.* **2020**, *126*, 103749. [[CrossRef](#)]
11. Holtstam, D.; Bindu, L.; Hälenius, U.; Andersson, U.B. Delhuyarite-(Ce)— $\text{Ce}_4\text{Mg}(\text{Fe}^{3+})_2\text{W}\square(\text{Si}_2\text{O}_7)_2\text{O}_6(\text{OH})_2$ —A new mineral of the chevkinite group, from the Nya Bastnäs Fe-Cu-REE deposit, Sweden. *Eur. J. Miner.* **2017**, *29*, 897–905. [[CrossRef](#)]
12. Ercit, T.S. Identification and alteration trends of granite-pegmatite-hosted (Y,REE,U,Th)-(Nb,Ta,Ti) oxide minerals: A statistical approach. *Can. Miner.* **2005**, *43*, 1291–1303. [[CrossRef](#)]
13. Aurisicchio, C.; De Vito, C.; Ferrini, V.; Orlandi, P. Nb-Ta oxide minerals from miarolitic pegmatites of the Baveno pink granite, NW Italy. *Miner. Mag.* **2001**, *65*, 509–522. [[CrossRef](#)]
14. Ferraris, G. Polymetasomatism as a tool for correlating properties and structure. In *Molecular Aspects of Minerals*; Merlini, S., Ed.; European Mineralogical Union: Budapest, Hungary, 1997; pp. 275–295.
15. Smith, M.P.; Henderson, P.; Campbell, L.S. Fractionation of the REE during hydrothermal processes: Constraints from the Bayan Obo Fe-REE-Nb deposit, Inner Mongolia, China. *Geochim. Cosmochim. Acta* **2000**, *64*, 3141–3160. [[CrossRef](#)]
16. Zozulya, D.; Lyalina, L.; Macdonald, R.; Bagiński, B.; Savchenko, Y.; Jokubauskas, P. Britholite group minerals from REE-rich lithologies of Keivy alkali granite—Nephelinesyenite complex, Kola Peninsula, NW Russia. *Minerals* **2019**, *9*, 732. [[CrossRef](#)]
17. Haas, J.R.; Shock, E.I.; Sassani, D.C. Rare earth elements in hydrothermal systems: Estimates of standard partial molal thermodynamic properties of aqueous complexes of the rare earth elements at high pressure and temperature. *Geochim. Cosmochim. Acta* **1995**, *59*, 4329–4350. [[CrossRef](#)]
18. Samson, I.M.; Wood, S.A. The rare earth element behavior in hydrothermal fluids and concentration in hydrothermal mineral deposits, exclusive of alkaline settings. *Geol. Assoc. Can. Short Course Notes* **2005**, *17*, 269–297.
19. Macdonald, R.; Bagiński, B.; Kartashov, P.M.; Zozulya, D.; Dzierżanowski, P.; Jokubauskas, P. Hydrothermal alteration of a chevkinite-group mineral to a bastnäsite-(Ce)-ilmenite-columbite-(Fe) assemblage: Interaction with a F-, CO₂-rich fluid. *Miner. Pet.* **2015**, *109*, 659–678. [[CrossRef](#)]
20. Li, X.-C.; Zhou, M.-F. Hydrothermal alteration of monazite-(Ce) and chevkinite-(Ce) from the Sin Quyen Fe-Cu-LREE-Au deposit, northwestern Vietnam. *Am. Miner.* **2017**, *102*, 1525–1541. [[CrossRef](#)]
21. Voloshin, A.V.; Pakhomovskii Ya, A. *Minerals and Evolution of Mineral Formation in Amazonite Pegmatites of the Kola Peninsula*; Nauka: Leningrad, Russia, 1986.
22. Stevenson, R.K.; Martin, R.F. Implications of the presence of amazonite in the Broken Hill and Geco metamorphosed sulfide deposits. *Can. Miner.* **1986**, *24*, 729–745.
23. Martin, R.; De Vito, C.; Pezzotta, F. Why is amazonitic feldspar an earmark of NYF-type granitic pegmatites? Clues from hybrid pegmatites in Madagascar. *Am. Miner.* **2008**, *93*, 263–269. [[CrossRef](#)]
24. Zozulya, D.R.; Kudryashov, N.M.; Lyalina, L.M.; Stepenshchikov, D.G. Late Archean rare-element pegmatites from Keivy-Kolmozero zone, Kola Peninsula, and dating (ID-TIMS, EMP) of pegmatitic zircon, microlite, monazite, and thorite. In Proceedings of the Magmatism of the Earth and Related Strategic Metal Deposits, Miass, Russia, 4–9 August 2017; Zaitsev, V.A., Ermolaeva, V.N., Eds.; Geokhi Ras: Moscow, Russia, 2017; pp. 332–334.
25. Bao, Z.; Al, T.; Couillard, M.; Poirier, G.; Bain, J.; Shrimpton, H.K.; Finfrock, Y.Z.; Lanzirotti, A.; Paktune, D.; Saurette, E.; Hu, Y.; et al. A cross-scale investigation of galena oxidation and controls on mobilization of lead in mine waste rock. *J. Hazard. Mater.* **2012**, *412*, 125130. [[CrossRef](#)]
26. El Alaoui, L.; Dekair, A. Theoretical study of the dissolution kinetics of galena and cerussite in an abandoned mining area (Zaida mine, Morocco). *E3S Web Conf.* **2018**, *37*, 01007. [[CrossRef](#)]
27. Droop, G.R. A general equation for estimating Fe³⁺ concentrations in ferromagnesian silicates and oxides from microprobe analyses, using stoichiometric criteria. *Miner. Mag.* **1987**, *51*, 31–435. [[CrossRef](#)]